COMMUNICATIONS IN COMPUTATIONAL PHYSICS
Vol. **4**, No. 3, pp. 496-505

Commun. Comput. Phys.
September 2008

Formation of Non-Maxwellian Distribution and Its Role in Collisionless Driven Reconnection

R. Horiuchi[1,2,*] and H. Ohtani[1,2]

[1] *National Institute for Fusion Science, Toki 509-52, Japan.*
[2] *The Graduate University for Advanced Studies, Toki 509-52, Japan.*

Received 29 October 2007; Accepted (in revised version) 30 November 2007

Available online 14 April 2008

Abstract. The dynamical evolution of collisionless driven reconnection is investigated by using an electromagnetic particle simulation code in a microscopic open system. Strong in-plane electrostatic field is excited in the central region of current sheet under the influence of an external driving field. As a result of the amplification of unmagnetized meandering motion by the electrostatic field particle distribution function is modified from the shifted Maxwellian to an anisotropic one in the current sheet. An ion hole appears at the center of current sheet in the phase space, where distribution becomes two-peaked and no ions exist in low velocity region between two peaks. The strong modification of distribution function leads to the generation of off-diagonal components of pressure tensor term, which is one of major causes to violate frozen-in constraint and trigger collisionless reconnection.

AMS subject classifications: 82D10,76E30,76W05,76X05

Key words: Collisionless reconnection, particle simulation, open system, multi-scale physics.

1 Introduction

Magnetic reconnection plays an important role in the dynamics of the solar flare, the magnetosphere, and laboratory experiments [1]. There are two key issues in considering magnetic reconnection. One is a local or microscopic issue. The excitation of magnetic reconnection needs a microscopic process, which leads to the generation of electric resistivity, such as wave-particle interaction [2–4], binary collisions, and so on. The other issue is a global or macroscopic issue. Magnetic reconnection results in global plasma transport and global change of field topology. Thus, magnetic reconnection is a multi-scale phenomenon bridging between macroscopic and microscopic hierarchies, and its whole

*Corresponding author. *Email addresses:* horiuchi.ritoku@nifs.ac.jp (R. Horiuchi), ohtani.hiroaki@nifs.ac.jp (H. Ohtani)

picture should be clarified by solving both microscopic physics and macroscopic physics consistently and simultaneously. We are now developing the multi-hierarchy simulation model for magnetic reconnection under MARIS (Magnetic Reconnection Interlocked Simulation) project. The simulation model consists of three parts, i.e., MHD model to describe global dynamics of reconnection phenomena, electromagnetic PIC model to describe the microscopic processes in the vicinity of reconnection point [5], and interface model to describe the interaction between micro and macro hierarchies [6].

Because microscopic reconnection system is just only a part of macroscopic system, microscopic open model is needed even for understanding of microscopic mechanism of magnetic reconnection. We have developed Particle Simulation code for Magnetic reconnection in an Open system (PASMO) [7–9], which is subject to an external driving source. This code is designed to be connected with a code for macroscopic system under the MARIS project, i.e., the information of macroscopic system is introduced into microscopic system through the system boundary. In this paper we discuss the microscopic physics of collisionless driven reconnection clarified by using PASMO code.

2 Open boundary model

Particle simulation code relies on the explicit electromagnetic PIC algorism [5]. As an initial condition we adopt a one-dimensional equilibrium with the Harris-type anti-parallel magnetic configuration as

$$\mathbf{B}(y) = (B_x(y),0,0), \tag{2.1}$$

$$B_x(y) = B_0 \tanh(y/L), \tag{2.2}$$

$$P(y) = B_0^2/8\pi \operatorname{sech}^2(y/L), \tag{2.3}$$

where B_0 is a constant and L is the scale height along the y-axis. There is a magnetically neutral sheet at $y=0$ in the initial equilibrium. The initial particle distribution is assumed to be a shifted Maxwellian with spatially constant temperature and average particle velocity, which is equal to the diamagnetic drift velocity.

In order to study the dynamical evolution of collisionless driven reconnection in an open system under the influence of an external driving source we have developed a new open boundary model, in which a free condition is used at the downstream boundary ($x=\pm x_b$) and an input condition is used at the upstream boundary ($y=\pm y_b$)) [7–10]. The boundary condition for the z-axis is assumed to be periodic. The plasma inflows are symmetrically driven from two upstream boundaries by the external electric field imposed in the z direction under the assumption that the frozen-in condition is satisfied for both ions and electrons. The driving field $E_{zd}(x,t)$ used for this simulation is the same as that in the previous simulations [7–10], which is controlled by two parameters, i.e., maximum flux input rate E_0 and the spatial size of initial bell-shaped profile x_d (input window size). The distribution function of incoming particles at the upstream boundary is assumed to

be a shifted Maxwellian with a constant temperature and the average velocity equal to the $\mathbf{E}\times\mathbf{B}$ drift velocity.

Field quantities E_x, E_y and $\partial E_z/\partial x$ are assumed to be continuous at the downstream boundary ($x=\pm x_b$). The condition $\partial E_z/\partial x=$ finite allows the change in the y-component of magnetic field which is the necessary condition for a magnetic island to go freely through the boundary. Magnetic field at the boundaries is directly given by solving Maxwell equations there. Using this boundary model we have succeeded in demonstrating intermittent reconnection in kinetic open system in which magnetic islands are frequently generated in the current sheet and move out through the downstream boundary [8]. The downstream boundary condition for particles is determined under the assumptions that charge neutrality is maintained and the distribution functions are the same as ones at one-grid inside position. There are three steps to realize the downstream boundary condition. First, extract particles within the distance of one grid from the boundary. Next, total number of particles within the distance of one grid from the boundary at new time step is determined so as to make the number flux continuous at the boundary. Third, the velocity and position of particles within the distance of one grid from the boundary at new time step are replaced using those of particles between the one-grid and two-grid distance from the boundary. Thus, not only outgoing particles but also incoming particles are allowed in this open boundary model. The physical importance of this condition is explained in the followings. The electron outflow with high velocity comparable to electron Alfven velocity is generated from electron dissipation region as a result of collisionless reconnection. When the electron outflow reaches the downstream boundary, strong electron return current should be supplied into the system to keep the charge neutrality, because the ion outflow velocity is usually much smaller than the electron one in the kinetic regime and so the ions cannot compensate for the loss of electron charge at the downstream boundary. Fig. 1 demonstrates the spatial profile of electron number flux in a steady state. It is clear in this figure that electron return current is formed along magnetic separatrix from the downstream boundary to the electron dissipation region.

Fig. 2 illustrates the spatial profiles of electron and ion frozen-in conditions obtained using developed three-dimensional simulation code ("PASMO"), where the simulation parameters are described in the next section, and the profiles are plotted after being averaged along the z direction. The frozen-in condition is clearly satisfied near the upstream boundary for both electrons and ions. This condition is slightly violated near the downstream boundary. Although we do not discuss the detailed mechanism here, the violation is due to the high velocity electron outflow and the return flow which can be described correctly in this open boundary model.

There is another approach for open particle boundary model [11], which has been developed for two-dimensional undriven reconnection. However, this approach is not applicable to the physics relating to a long time behavior of reconnection such as steady reconnection and intermittency in reconnection because there is no external energy source to sustain reconnection for a long time. Furthermore, three-dimensional model is needed

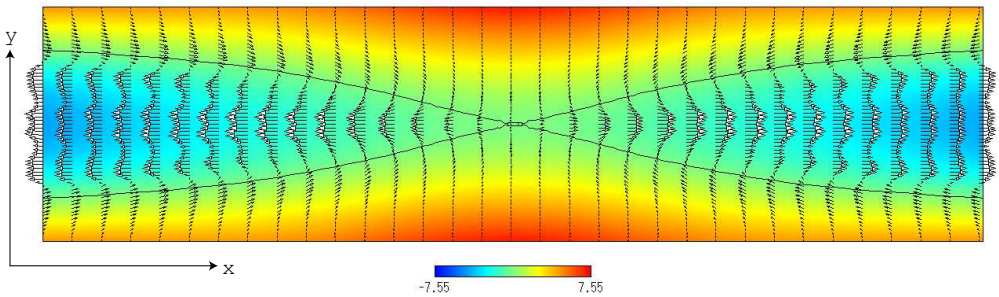

Figure 1: Spatial profile of electron number flux in the (x,y) plane at $\omega_{ce}t=862$, where color contours stand for average magnetic flux A_z.

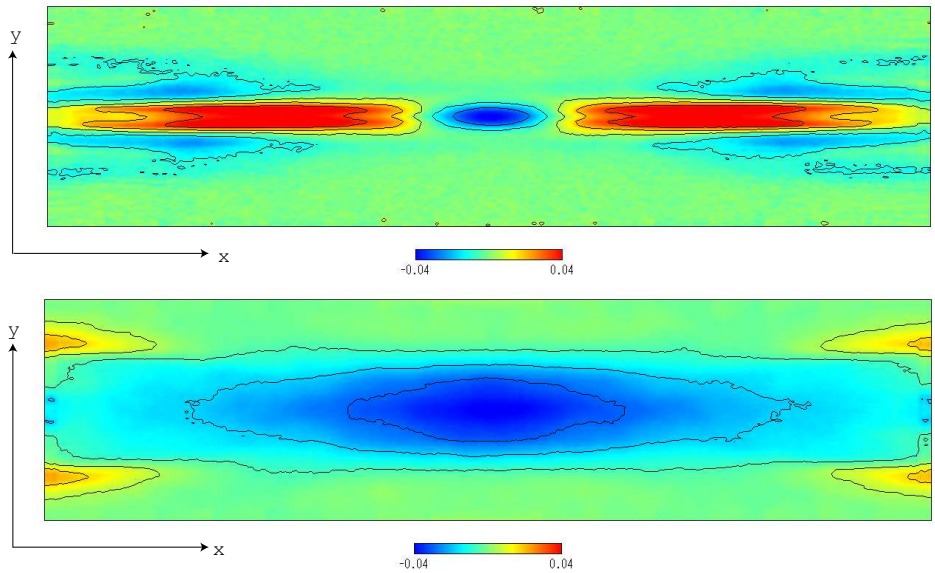

Figure 2: Spatial profile of electron frozen-in condition $\mathbf{E}+\mathbf{v_e}\times\mathbf{B}$ (top) and ion frozen-in condition $\mathbf{E}+\mathbf{v_i}\times\mathbf{B}$ (bottom) in the (x,y) plane at $\omega_{ce}t=682$, where red and blue colors stand for positive and negative values, respectively.

to clarify the relationship of two triggering mechanisms, which is a hot issue in collisionless reconnection, i.e., particle kinetic effect [7–10, 13, 14] and anomalous resistivity due to plasma instabilities [2–4, 12, 15].

3 Simulation results

We carry out a long simulation run using three-dimensional version of PASMO code. The simulation runs for the numerical check of PASMO code have been reported in a series of papers [7–10]. This paper is focus on the microscopic physics in a steady state

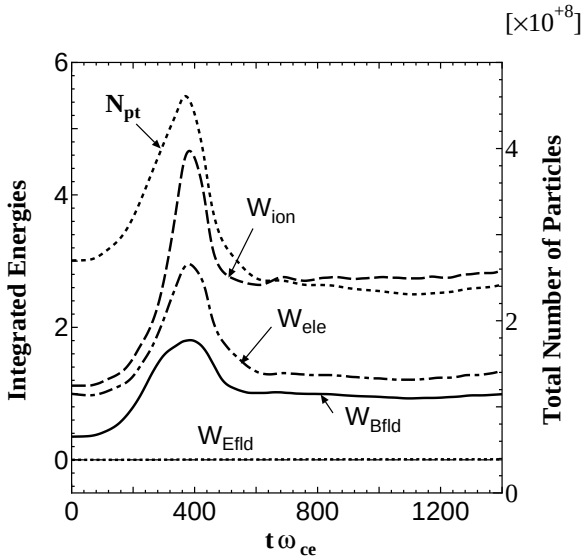

Figure 3: Temporal evolutions of integral energies and total number of particles, where magnetic energy, electric field energy, ion energy and electron energy are plotted by solid, dotted, dashed, dot-dashed lines, respectively. Right vertical axis measures total number of particles used for simulation.

obtained from a typical long simulation run. The important parameters are as follows; the total number of particles used for the present simulation is about 560 000 000, and the simulation domain is implemented on a $(256\times129\times128)$ point grid, the ratio of ion to electron temperature is $T_i/T_e=1$, the ion Larmor radius associated with a magnetic field outside the current layer is $\rho_i=0.93L$, and the ratio of the electron drift velocity to the electron thermal velocity is $v_{ze}/v_{te}=0.21$, $m_i/m_e=50$, and $\omega_{pe}/\omega_{ce}=2.5$. The physical quantities used in this simulation are normalized by the light velocity c for velocity, c/ω_{ce} for spatial scale, and $1/\omega_{ce}$ for time. The simulation box size is $2x_b\times2y_b\times2z_b=34.6c/\omega_{ce}\times11.5c/\omega_{ce}\times17.3c/\omega_{ce}$. Total number of simulation time steps is 34,000 , which corresponds to the physical time of $\omega_{ce}t=1494$. Temporal evolutions of integral energies and total number of particles are plotted in Fig. 3. The system relaxes to a steady state after an initial transit phase ($\omega_{ce}t>600$). That is, the energy inflow rate into the system is balanced with the energy outflow rate from the system. Although total number of particle in the system, N_{pt}, is a function of time, its value is almost constant in a steady state.

Two kinds of plasma instabilities are observed to excite in the current sheet, i.e., lower hybrid drift instability (LHDI) [2] and drift kink instability (DKI) [3, 4, 12]. These waves propagate along the out-of-plane direction (z-axis) and form three-dimensional structure in the current sheet. The LHDI grows in the periphery of the current sheet in an early phase, but it saturates nonlinearly and damps in the steady state. The DKI starts to grow slowly in the central region of current sheet after the LHDI saturates, and it becomes visible in the late phase of the simulation ($\omega_{ce}t>1200$). Thus, two-dimensional structure of the current sheet is maintained in the steady state.

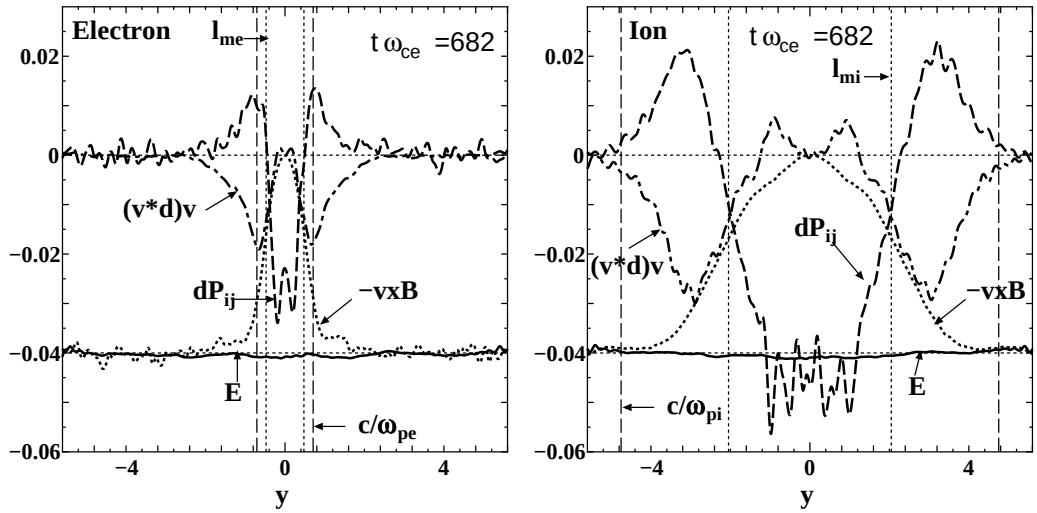

Figure 4: Spatial profiles of non-ideal terms for electrons (left) and ions (right) along the y-axis at $\omega_{ce}t=682$, where the y-axis is normalized by c/ω_{ce}.

3.1 Violation of frozen-in condition

Kinetic regime appears in the central current layer, in which frozen-in condition is broken due to kinetic processes, as shown in Fig. 2. Kinetic regime consists of two dissipation regions with different spatial scales, i.e., ion dissipation region (IDR) and electron dissipation region (EDR) [7, 10, 13]. It is useful for us to discuss the violation of frozen-in condition by using non-ideal terms in two-fluid equations as

$$n_j q_j(\mathbf{E}+\mathbf{u_j}\times\mathbf{B}) = m_j n_j(\frac{\partial}{\partial t}+\mathbf{u}_j\cdot\nabla)\mathbf{u}_j+\frac{\partial\bar{\mathbf{P}}_j}{\partial\mathbf{x}}+\frac{\partial p_j}{\partial\mathbf{x}}, \tag{3.1}$$

where the subscript j ($=i,e$) denotes ion or electron, $\bar{\mathbf{P}}_j$ and $\mathbf{u}_j$ are pressure tensor and fluid velocity, respectively. Spatial profiles of z-component of non-ideal terms for electrons (left) and ion (right) along the y-axis are plotted in Fig. 4. The z-component of electric field becomes uniform in a steady state (solid curve). That is, the input rate of magnetic flux at the upstream boundary is balanced with the reconnection rate. Pressure tensor term becomes dominant in the vicinity of reconnection point ($y=0$) for both electrons and ions. Because the off-diagonal component of pressure tensor terms are originated from the non-gyrotropic motion in the vicinity of neutral sheet, "meandering motion", the spatial size for the violation of frozen-in condition is given by meandering motion amplitude. The average amplitude of meandering motion is given by the distance which satisfies the condition as

$$\rho(y)=y, \tag{3.2}$$

where $\rho(y)$ is local Larmor radius at the distance y from the neutral sheet. Thus, the violation of frozen-in condition is caused mainly by pressure tensor term. These results are consistent with those in the previous simulations [7–10, 14].

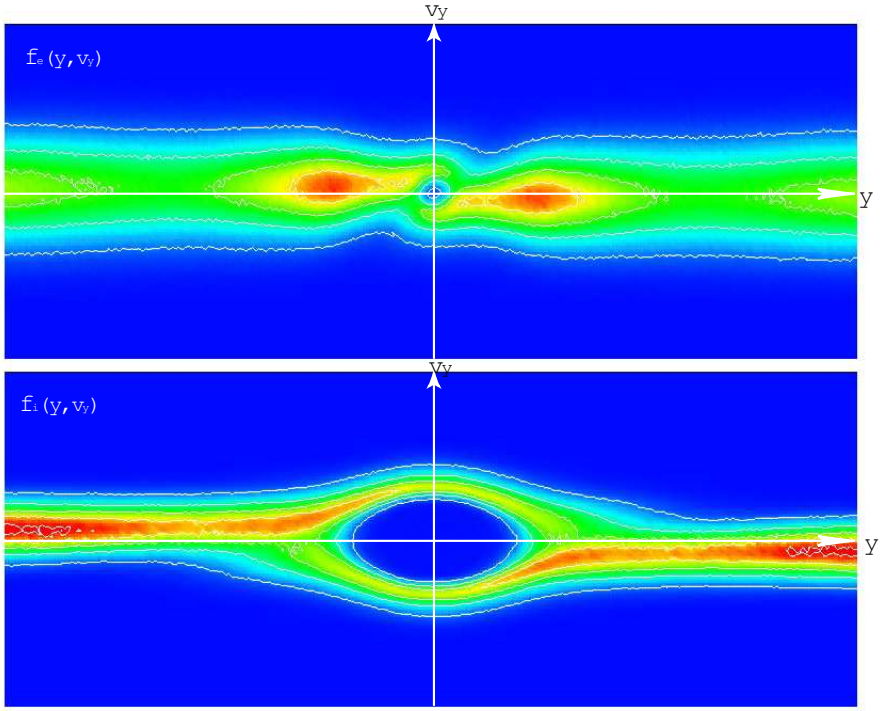

Figure 5: Distribution functions of electrons (top) and ions (bottom) in phase space (y,v_y) at $\omega_{ce}t=637$, where red color stands for a high value.

3.2 Formation of non-Maxwellian distribution function

Let us examine the violation frozen-in condition in more detail, based on particle distribution function. Initial particle distribution is given by the shifted Maxwellian. Fig. 5 shows the distribution functions of electrons (top) and ions (bottom) in phase space (y,v_y) at $\omega_{ce}t=637$, where the reconnection point is located at the center of y-axis (horizontal axis). The particles which satisfy the shifted Maxwellian distribution are supplied into the system from the upstream boundaries (left and right boundaries in Fig. 5). The distribution functions near the reconnection point are largely modified in a quite different form. A big ion hole appears in the center of phase space where there exist no ions, while a small electron hole is formed inside the EDR. The spatial size of modified region is given by the meandering amplitude.

Let us examine the detailed mechanism to create ion and electron holes in the current sheet. Because ions are not magnetized inside the IDR, the driving field pushes magnetized electrons strongly inward there and electron-rich region is formed inside the EDR (see solid curve in Fig. 6). The spatial size of electron-rich region is given by the electron skin depth c/ω_{pe}. The in-plane electrostatic field (dashed curve) is generated due to the charge separation, and ion inflow motion is accelerated toward the neutral sheet by

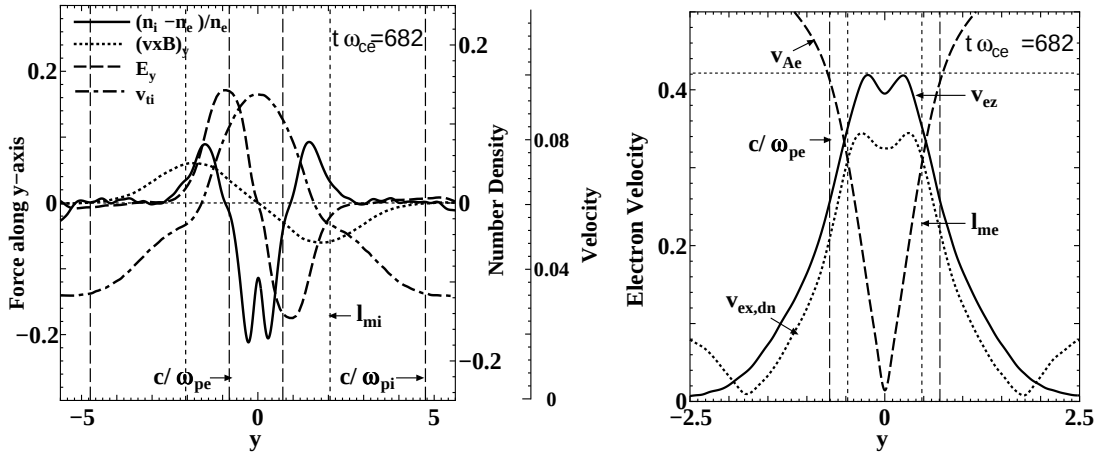

Figure 6: Spatial profiles of normalized charge density, forces acting ions, and ion thermal velocity (left), those of electron velocities (right) at $t\omega_{ce}=682$, where ion thermal velocity is defined by the standard deviation of ion velocity distribution, and the y-axis is normalized by c/ω_{ce}.

the electrostatic field. The dot-dashed curve in the left panel of Fig. 6 denotes the standard deviation of ion velocity distribution, which corresponds to the ion thermal velocity for the shifted Maxwellian near the upstream boundary, but to the average meandering speed inside the ion hole. This figure suggests that the ion meandering speed inside the ion hole becomes three times larger than ion thermal velocity at the upstream boundary. Thus, inward ion meandering motion is amplified by the in-plane electrostatic field and ion hole structure is formed coherently in the phase space. The strong modification of distribution function from the shifted Maxwellian to non-Maxwellian with ion and electron holes leads to the generation of off-diagonal components of pressure tensor term, because

$$\frac{\partial}{\partial y}\left[\int (v_y-u_y)(v_z-u_z)f(y,\mathbf{v})d\mathbf{v}\right]=\text{finite} \tag{3.3}$$

inside the dissipation region. This term plays an important role in violating frozen-in constraint and triggering collisionless reconnection, as shown in Fig. 4.

3.3 Particle acceleration and heating

Because electrons becomes unmagnetized in the EDR, they are accelerated along the z-axis by the reconnection electric field as soon as they enter into the EDR. The right panel of Fig. 6 shows the spatial profiles of electron velocities at $t\omega_{ce}=682$. The out-of-plane component of electron average velocity (solid) reaches the electron Alfven velocity (dashed) evaluated at the edge of the EDR. This result implies that most of magnetic energy carried into the EDR is converted into the electron kinetic energy. The ions are also accelerated inside the IDR in the same way. Top panels of Fig. 7 are the distribution functions of electrons (left) and ions (right) in phase space (y,v_z) at $t\omega_{ce}=637$. It is clearly seen in Fig. 7 that the electron acceleration along the out-of-plane direction tales place

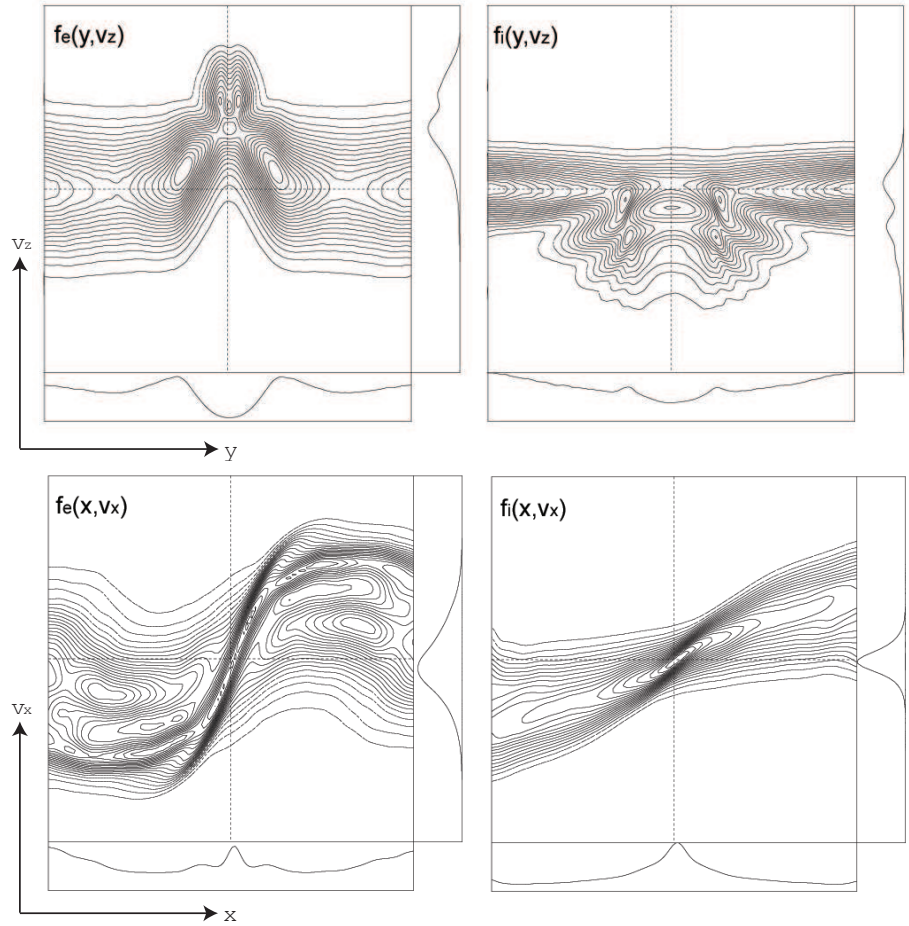

Figure 7: Distribution functions of electrons (left) and ions (right) along the inflow direction (top) and the outflow direction (bottom) at $t\omega_{ce}=637$.

inside the EDR, while the ion acceleration takes place inside the IDR. The strong $\mathbf{j}\times\mathbf{B}$ force associated with resultant reconnection current (j_z) and the reconnected magnetic field (B_y) accelerates electrons toward the outflow direction (x-axis) and its speed (dotted curve in the right panel of Fig. 6) becomes comparable to the electron Alfven velocity at the downstream edge of the EDR [13]. Here, the downstream edge of the EDR is defined by the position where the electron outflow speed becomes maximum. Bottom panels of Fig. 7 are the distribution functions of electrons (left) and ions (right) in phase space (x,v_x) at $t\omega_{ce}=637$. The oblique peaked profile of electron distribution extends to the downstream edge of the EDR. The z-component of electron kinetic energy is converted into its x-component in this acceleration process. The distribution becomes wider as soon as they move out of the EDR. Thus, the electron thermalization takes place in the IDR as well as the ion thermalization.

4 Summary

The dynamical evolution of collisionless driven reconnection is investigated by using an electromagnetic particle simulation code in a microscopic open system (PASMO). The plasma inflows, which satisfies a shifted Maxwellian, are symmetrically driven from two upstream boundaries by imposing the external electric field in the z direction. The existence of two dissipation regions, i.e., ion and electron dissipation regions, with different spatial size leads to the charge separation under the influence of an external driving field. The resultant in-plane electrostatic field amplifies ion unmagnetized thermal motion called meandering motion. Consequently, particle distribution function is modified from the shifted Maxwellian to an anisotropic one. An ion hole of the ion meandering spatial scale appears at the center of current sheet in the phase space, where velocity distribution becomes two-peaked and no ions exist in low velocity region between two peaks. In the same way an electron hole with the spatial size of electron meandering motion appears in the electron phase space. The strong modification of distribution function leads to the generation of off-diagonal components of pressure tensor term, which is one of major causes to violate frozen-in constraint and trigger collisionless reconnection.

Acknowledgments

This work was partially supported by a Grant-in-Aid for Scientific Research from the Japan Society for the Promotion of Science (No. 18340188), the Research Cooperation Program on Hierarchy and Holism in Natural Sciences 2 at National Institutes of Natural Sciences, and General Coordinated Research at National Institute for Fusion Science (NIFS06KTAT037).

References

[1] M. Yamada, Phys. Plasma 14 (2007) 058102-1-16.
[2] N. A. Krall, P. C. Liewer, Phys. Rev. 4 (1971) 2094.
[3] Z. Zhu, R. M. Winglee, J. Geophys. Res. 101 (1996) 4885.
[4] R. Horiuchi, T. Sato, Phys. Plasmas 6 (1999) 4565-4574.
[5] C. K. Birdsall, A. B. Langdon, Plasma Physics via Computer Simulation, McGraw-Hill, New York, 1985.
[6] S. Usami, H. Ohtani, R. Horiuchi, M. Den, Commun. Comput. Phys. 4 (2008) 537-544.
[7] W. Pei, R. Horiuchi, T. Sato, Phys. Rev. Lett. 87 (2001) 235003-1-235003-4.
[8] W. Pei, R. Horiuchi, T. Sato, Phys. Plasmas 8 (2001) 3251-3257.
[9] R. Horiuchi, H. Ohtani, A. Ishizawa, Comput. Phys. Commun. 164 (2004) 17-22.
[10] A. Ishizawa, R. Horiuchi, Phys. Rev. Lett. 95 (2005) 045003-1-045003-4.
[11] W. Daughton, J. Schdder, H. Karimabadi, Phys. Plasmas 13 (2006) 072101.
[12] T. Moritaka, R. Horiuchi, H. Ohtani, Phys. Plasmas 14 (2007) 102109.
[13] M. A. Shay, J. F. Drake, B. N. Rogers, R. E. Denton, J. Geophys. Res. 106 (2001) 3759.
[14] M. Hesse, K. Schindler, J. Birn, M. Kuznetsova, Phys. Plasmas 6 (1999) 1781.
[15] W. Daughton, Phys. Plasmas 6 (1999) 1329.